The Astrophysical Journal Letters, 746:L17 (5pp), 2012 February 20 doi:10.1088/2041-8205/746/2/L17

DEFINING THE "BLIND SPOT" OF *HINODE* EIS AND XRT TEMPERATURE MEASUREMENTS

Amy R. Winebarger[1], Harry P. Warren[2], Joan T. Schmelz[3], Jonathan Cirtain[1], Fana Mulu-Moore[1], Leon Golub[4], and Ken Kobayashi[5]
[1] NASA Marshall Space Flight Center, VP 62, Huntsville, AL 35812, USA; amy.r.winebarger@nasa.gov
[2] Space Science Division, Naval Research Laboratory, Washington, DC 20375, USA
[3] Physics Department, University of Memphis, Memphis, TN 38152, USA
[4] Harvard-Smithsonian Center for Astrophysics, 60 Garden St., Cambridge, MA 02138, USA
[5] Center for Space Plasma and Aeronomic Research, 320 Sparkman Dr, Huntsville, AL 35805, USA
Received 2011 June 13; accepted 2011 December 21; published 2012 January 30

ABSTRACT

Observing high-temperature, low emission measure plasma is key to unlocking the coronal heating problem. With current instrumentation, a combination of EUV spectral data from *Hinode* Extreme-ultraviolet Imaging Spectrometer (EIS; sensitive to temperatures up to 4 MK) and broadband filter data from *Hinode* X-ray Telescope (XRT; sensitive to higher temperatures) is typically used to diagnose the temperature structure of the observed plasma. In this Letter, we demonstrate that a "blind spot" exists in temperature–emission measure space for combined *Hinode* EIS and XRT observations. For a typical active region core with significant emission at 3–4 MK, *Hinode* EIS and XRT are insensitive to plasma with temperatures greater than ∼6 MK and emission measures less than $\sim 10^{27}$ cm^{-5}. We then demonstrate that the temperature and emission measure limits of this blind spot depend upon the temperature distribution of the plasma along the line of sight by considering a hypothetical emission measure distribution sharply peaked at 1 MK. For this emission measure distribution, we find that EIS and XRT are insensitive to plasma with emission measures less than $\sim 10^{26}$ cm^{-5}. We suggest that a spatially and spectrally resolved 6–24 Å spectrum would improve the sensitivity to these high-temperature, low emission measure plasma.

Key word: Sun: corona

1. INTRODUCTION

Since the discovery of million-degree coronal temperatures by Elden and Grotrian in the 1930s, the major problem in coronal physics has been to determine the mechanisms that transfer and dissipate energy into the corona. For instance, one popular theory suggested by Parker (1972) is that photospheric motions braid and stress magnetic field lines in the corona. This stored energy is then released through magnetic reconnection. The energy released in each reconnection event, termed a "nanoflare," is thought to be short-lived and of a small magnitude. As it turns out, regardless of the transfer or dissipation mechanism, the predicted timescale for energy release for all mechanisms is finite, i.e., a single heating event is relatively short-lived (Klimchuk 2006). The *frequency* of heating events on a single strand in the corona, however, is unknown. (Here we use the term "strand" to refer to the fundamental flux tube in the corona and the term "loop" to refer to a coherent structure in an observation. A loop can consist of a single strand, or many, sub-resolution strands.) Knowledge of the frequency of the heating events would provide significant constraints on the coronal heating mechanism: low-frequency (or sporadic) heating might support a reconnection or stressing mechanism, while high-frequency (quasi-steady) heating is more likely to support a wave heating mechanism.

It is difficult to determine the frequency of heating events from the steadiness of the intensities and velocities of active region structures because both low- and high-frequency heating can predict those observational characteristics (see Klimchuk 2009 and reference therein). One observation that can discriminate between low- and high-frequency heating in active region cores is the presence of high-temperature plasma. If the heating in a strand is high frequency, the temperature of that strand remains relatively constant because the strand does not have a chance to cool and drain between heating events. In contrast, if the heating in an active region core is low frequency, meaning a strand has the opportunity to cool and drain between heating events, higher temperature plasma would be present (Klimchuk 2006, 2009; Klimchuk et al. 2008; Mulu-Moore et al. 2011). The amount of high-temperature emission is controlled by the density in the loop at the time of the heating event as well as the resulting time-dependent ionization equilibrium (Bradshaw & Klimchuk 2011). Using the observed loop lengths and pressure at the loop footpoints, it is possible to determine the maximum temperature that can be generated by high-frequency heating (Winebarger et al. 2011). If plasma is detected at temperatures larger than can be supported by high-frequency (steady) heating, some of the heating in the active region core must be low frequency (sporadic). If, on the other hand, high-temperature plasma is absent, the heating must be high frequency.

It has long been recognized that measuring high-temperature, low emission measure (EM) plasma is a difficult task (e.g., Martens et al. 1985); however, recent analyses have hinted at the possibility of a hot plasma component to active regions (Schmelz et al. 2009a, 2009b; Reale et al. 2009; Shestov et al. 2010). Unfortunately, the ability of current instrumentation, such as *Hinode*'s X-ray Telescope (XRT) or Extreme-ultraviolet Imaging Spectrometer (EIS), to detect high-temperature, low EM plasma in active region cores is limited. In this Letter, we quantitatively define the temperatures and EMs that are *not* being sampled by *Hinode* XRT and EIS. We illustrate this using observations of active region 11089 obtained on 2010 July 23 (Warren et al. 2011). We find that for the observed active region core, *Hinode* EIS and XRT are insensitive to plasma with temperatures greater than ∼6 MK and EMs less than $\sim 10^{27}$ cm^{-5}. We then consider a hypothetical EM distribution that is sharply peaked at 1 MK. For this EM distribution, *Hinode*

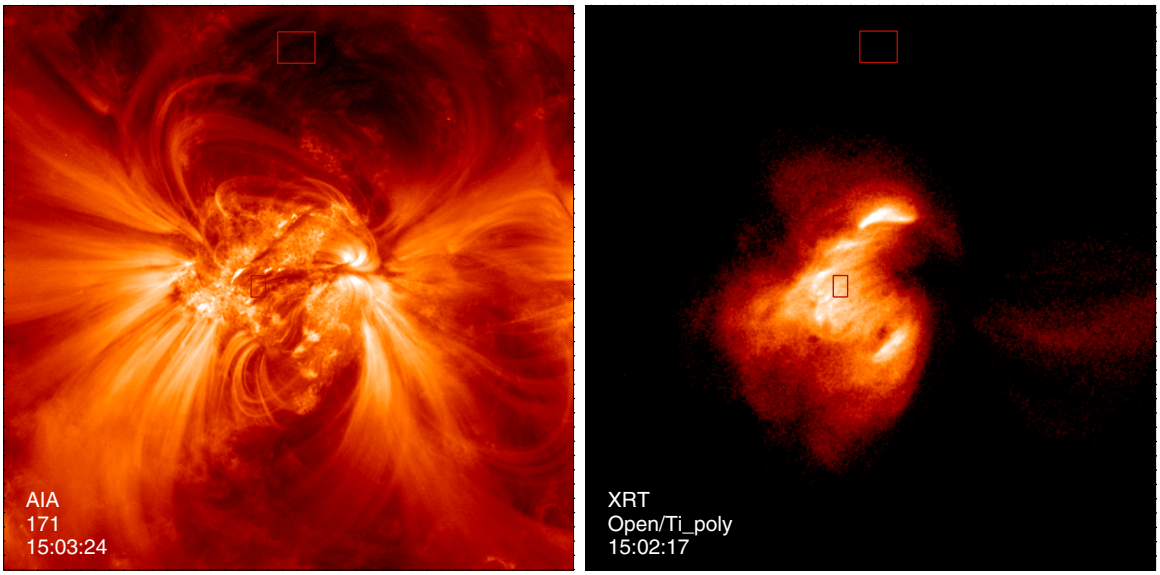

Figure 1. Active region 11089 observed on 2010 July 23. The *Solar Dynamics Observatory*/Atmospheric Imaging Assembly 171 Å image on the left shows an arcade of warm (∼1 MK) coronal loops around the footpoints of the hot loops which form the reticulated pattern in the center of the image. Hot core loops are bright in the *Hinode*/XRT Ti-poly filter image on the right. There are two boxes drawn on the images, one in the core of the active region over the neutral line and one away from the core that will be used to estimate the background.

EIS and XRT are more sensitive to high-temperature, low EM plasma. In the discussion section, we argue that a spatially and spectrally resolved spectrum in 6–24 Å, as proposed for the Marshall Grazing Incidence X-ray Spectrometer (MaGIXS; Kobayashi et al. 2010), would improve our ability to diagnose high-temperature, low EM plasma.

2. ANALYSIS

In this Letter, we present an analysis of the *Hinode* XRT and EIS data of active region 11089 observed on 2010 July 23. An analysis of this active region, including a description of the data, analysis techniques, and alignment between the EIS and XRT data sets, was previously presented in Warren et al. (2011). We use the active region core intensity measurements given by Warren et al. (2011) with two key changes. We use a region away from the active region core to calculate the background (in Warren et al. 2011, there was no background subtraction) and we revisit the uncertainties of the XRT intensities. The region of interest and the region used for background calculation are shown in Figure 1. The intensities averaged over the core region and the background region with their statistical uncertainties are given in Columns 2 and 3 of Table 1.

When the EIS lines are fit, the error in the intensity due to photon noise and the fitting procedure is calculated. The statistical error (given in Columns 2 and 3 of Table 1) is then combined with the systematic uncertainties in the instrument response and degradation, which is determined to be 22% of the original (non-background subtracted) intensities (Lang et al. 2006). The background subtracted intensities and errors are given in Column 4 of Table 1. Because XRT is a broadband instrument, the uncertainties in the data due to photon noise are more difficult to characterize. We use a bootstrap method (see Winebarger et al. 2011) to determine the statistical uncertainties. We first calculate the differential emission measure (DEM) from the EIS and XRT intensities using the method described below. We then calculate the emergent spectrum from the DEM. The photon noise can then be calculated directly from the spectrum. We combine this photon noise with an assumed 20% systematic uncertainty in the instrument calibration and degradation. This systematic uncertainty is based on a combination of known experimental errors and rough estimates of systematic errors. The uncertainties given in Column 4 of Table 1 represent the final uncertainties from the bootstrap calculation and systematic errors.

To generate possible DEM curves that can reproduce the observed fluxes given in Table 1, we have used `xrt_dem_iterative2.pro` (Golub et al. 2004; Weber et al. 2004), which was designed originally for use with XRT data only but has been modified slightly to allow for inclusion of EIS data as well. The routine employs a forward-fitting approach where a DEM is guessed and folded through each response to generate predicted fluxes. The DEM is interpolated from several spline knots. This process is iterated to reduce the χ^2 between the predicted and observed fluxes. This routine uses Monte Carlo iterations to estimate uncertainties in the DEM solution. For each iteration, the observed flux in each filter or line was varied randomly within the uncertainties and the program was run again with the new values. The `xrt_dem_interative2.pro` program requires user input for the XRT response functions and EIS emissivity functions. The XRT filter responses were calculated using the XRT standard software (`make_xrt_wave_resp.pro` and `make_xrt_temp_resp.pro`). These programs account for the time-dependent contamination of the XRT CCD and incorporate the latest XRT calibration data (Narukage et al. 2011). The EIS line emissivity functions were calculated using CHIANTI 6.0.1 (Dere et al. 2009). Coronal abundances (Feldman et al. 1992) and the default CHIANTI ionization equilibrium were used. The emissivity function for some ions is density sensitive. As a default, we find a density from the Fe XIII 202.044/203.826 Å intensity ratio. The ratio of the two intensities given in Table 1 return a density of $\log n_e = 9.6\,\mathrm{cm}^{-3}$. All emissivity functions were calculated using this density.

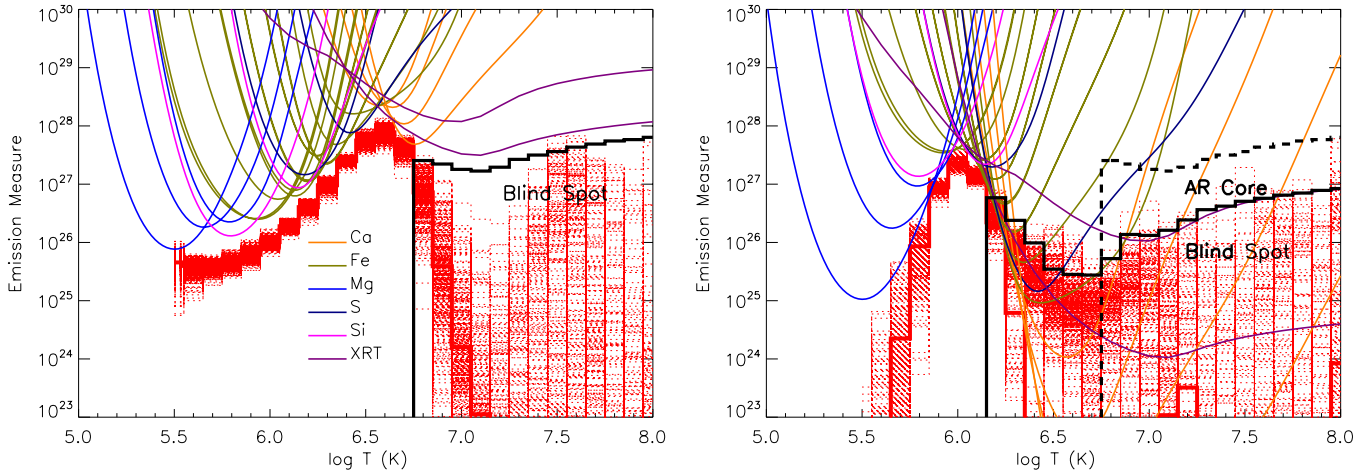

Figure 2. Left panel: the emission measure curve (thick red line) determined from the intensities of 21 EIS spectral lines and 2 XRT filter images of the active region core shown in Figure 1. The dotted red lines around the primary EM curve were calculated by varying the intensities within the uncertainties. The black line traces out the amount of emission that can be added to a single bin without increasing the modeled intensities by more than the errors. This demonstrates that this data set has a "blind spot" for plasma at temperatures greater than $\log T = 6.8$ and EM less than 10^{27} cm^{-5}. Right panel: the emission measure distribution for a hypothetical cool structure. If only 1 MK plasma is along the line of sight, these instruments are more sensitive to high-temperature plasma. When comparing the blind spot of this DEM (thick black line) to that of the active region core (dashed line), it is broader and at lower emission measures.

Table 1
EIS and XRT Intensities for Active Region Core

Line/Filter	I_{obs}	I_{back}	I_{core}	I_{DEM}	Ratio
Mg v 276.579 Å	16.49 ± 1.06	1.81 ± 0.58	14.68 ± 5.35	16.41	0.89
Mg vi 270.394 Å	35.91 ± 0.65	2.14 ± 0.20	33.77 ± 11.21	21.50	1.57
Fe ix 188.497 Å	72.40 ± 1.72	7.12 ± 0.30	65.28 ± 22.66	74.77	0.87
Fe ix 197.862 Å	40.00 ± 0.80	5.29 ± 0.18	34.71 ± 12.50	41.99	0.83
Mg vii 280.737 Å	32.70 ± 1.55	1.64 ± 0.26	31.06 ± 10.41	19.01	1.63
Si vii 275.368 Å	46.96 ± 1.16	4.28 ± 0.31	42.68 ± 14.70	53.25	0.80
Fe x 184.536 Å	280.38 ± 3.86	34.84 ± 1.01	245.54 ± 87.40	190.32	1.29
Fe xi 188.216 Å	578.24 ± 3.03	87.58 ± 0.67	490.66 ± 179.96	407.20	1.20
Fe xii 192.394 Å	437.81 ± 2.03	60.34 ± 0.41	377.47 ± 136.24	333.33	1.13
Fe xi 180.401 Å	926.12 ± 13.03	150.15 ± 3.52	775.97 ± 288.73	807.82	0.96
S x 264.233 Å	71.77 ± 1.68	9.58 ± 0.46	62.19 ± 22.46	63.46	0.98
Si x 258.375 Å	293.96 ± 3.09	25.88 ± 0.83	268.08 ± 91.56	257.50	1.04
Fe xii 195.119 Å	1475.39 ± 4.16	224.97 ± 0.76	1250.42 ± 459.07	1038.40	1.20
Fe xiii 202.044 Å	1248.29 ± 5.56	270.00 ± 1.42	978.29 ± 388.46	485.33	2.02
Fe xiii 203.826 Å	2533.87 ± 12.30	78.02 ± 1.57	2455.85 ± 788.55	1181.47	2.08
Fe xv 284.160 Å	10334.03 ± 20.41	217.85 ± 1.93	10116.18 ± 3215.32	13061.28	0.77
Fe xiv 270.519 Å	515.05 ± 2.66	22.15 ± 0.46	492.90 ± 160.29	582.61	0.85
Fe xiv 264.787 Å	1026.91 ± 4.20	34.37 ± 0.59	992.54 ± 319.55	1220.11	0.81
Fe xvi 262.984 Å	1157.60 ± 4.74	7.99 ± 0.41	1149.61 ± 360.22	1051.22	1.09
S xiii 256.686 Å	854.66 ± 5.44	11.00 ± 0.79	843.66 ± 266.02	955.13	0.88
Ca xiv 193.874 Å	311.91 ± 1.87	0.12 ± 0.06	311.79 ± 97.08	203.18	1.53
Ca xv 200.972 Å	238.92 ± 2.54	0.10 ± 1.00	238.82 ± 74.42	148.33	1.61
Ca xvi 208.604 Å	121.96 ± 8.85	0.10 ± 1.00	121.86 ± 39.96	106.51	1.14
Ca xvii 192.858 Å	146.54 ± 2.64	0.55 ± 0.32	145.99 ± 45.75	174.82	0.84
Ti-poly	1854.29 ± 372.51	6.50 ± 1.30	1847.79 ± 630.51	1208.60	1.53
Al-thick	4.48 ± 0.90	0.10 ± 0.10	4.38 ± 2.21	5.70	0.77

Figure 2 shows the results of the DEM calculation for the active region core in the left panel. The thick red line shows the EM distribution, $\xi(\log T)dT$, where $\xi(\log T)$ is the DEM calculated from the intensities given in Table 1 and $dT = (T/\log e)d\log T$. We have used $d\log T = 0.1$. The EM Loci curves are shown for the observed intensities and are color coded for the different elements and filters. The dotted red lines clustered around the solid thick red line are EM curves calculated by varying the input intensities within the uncertainties and hence provide an estimate of the uncertainty in the EM curve. For temperatures where the dotted lines tightly cluster around the primary EM curve (i.e., $5.5 \leqslant \log T \leqslant 6.7$), the EM is thought to be well constrained by the available data.

We now calculate how much additional emission can be added to a *single* temperature bin without increasing the modeled intensities (I_{DEM} in Column 5 of Table 1) in any spectral line or filter by more than the calculated errors (σ, given in Column 4 of Table 1). To the primary DEM, $\xi(\log T)$, we add a step function centered on a single temperature bin, i.e.,

$$\xi_{new}(\log T) = \xi(\log T) + C_i\delta(\log T_i). \quad (1)$$

From the new DEM, we calculate new intensities, I_{new}, and compare them to the original intensities, I_{DEM}. We increase C_i until the new intensities are greater than the original intensities plus the errors in at least one spectral line or filter, i.e., $I_{new} > I_{DEM} + \sigma$. We determine a value of C for each temperature bin. The curve that defines the amount of additional emission that could be added to each individual bin is

$$\epsilon_{BS}(\log T) = \xi(\log T) + C(\log T). \quad (2)$$

Note that this curve, $\epsilon_{BS}(\log T)$, is *not* an EM curve; rather, it is a curve that defines the upper limit of the additional emission that can be added to each bin when considered individually. For temperature bins where the EM curve is well constrained, $\epsilon_{BS}(\log T)$ is only slightly larger than $\xi(\log T)$, i.e., adding a small amount of additional emission into that bin changes the modeled intensities by more than 1σ. For temperatures where the EM is poorly constrained, we find we can add significant emission to a single temperature bin without greatly effecting the modeled intensities. In the left panel of Figure 2, we show $\epsilon_{BS}(T)dT$ with a thick black line. We only plot the curve for temperature bins where $\epsilon_{BS}(\log T) > 2\xi(\log T)$. For instance, the EM at 10 MK determined from the observed intensities is 1.6×10^{24} cm^{-5}. We find we could increase the EM in that bin to 1.8×10^{27} cm^{-5} (a factor of 1000) without changing the modeled intensities by more than 1σ. These results show that the available observations have a blind spot in temperature–EM space; they cannot detect low emission measure (EM $\lesssim 10^{27}$ cm^{-5}), high-temperature ($T \geqslant 6$ MK) plasma in an active region core.

To investigate how the blind spot depends upon the temperature of the plasma along the line of sight, we next consider a hypothetical DEM distribution that a Gaussian function centered at 1 MK with a width of 0.6 in $\log T$. We choose the magnitude of this DEM to be 1×10^{24} cm^{-5} K^{-1} so that the intensity in the Fe XII lines is approximately equal to the intensity in Fe XII in the active region core. This type of distribution would be representative of active region fan structures or the quiet Sun. From our assumed distribution, we calculate the expected EIS and XRT intensities for the same set of lines observed for the active region core; these intensities are given in Table 2. For many of the spectral lines, these intensities are approximately 0 and would be immeasurable, hence we cannot calculate the uncertainties by taking a percentage of the intensities. For these low-intensity values, we use three times the average intensity in the background region shown in Figure 1 as the uncertainty in the intensity. The resulting errors are given in Table 2. Note that for hot ions and XRT filters, the predicted intensities are significantly less than the errors. The EM distribution calculated from this set of intensities is shown in the right panel of Figure 2. The blind spot curve is shown as a thick black line. For this EM distribution, we find that the combined *Hinode* EIS and XRT is more sensitive to high-temperature, low EM plasma. For instance at 10 MK, we can now detect emission measure $>1.3 \times 10^{26}$ cm^{-5} which is an order of magnitude better than the active region core example. When compared to the blind spot curve of the active region core (shown in the right panel of Figure 2 as a thick dashed line), the blind spot is broader and at lower EMs. Hence if only cool emission is along the line of sight, it is easier to detect high-temperature, low EM plasma.

Table 2
EIS and XRT Intensities for Hypothetical Cool Region

Line/Filter	I_{cool}	I_{DEM}	Ratio
Mg V 276.579 Å	2.07 ± 5.43	2.04	1.01
Mg VI 270.394 Å	33.20 ± 6.64	33.20	1.00
Fe IX 188.497 Å	879.00 ± 176.00	878.00	1.00
Fe IX 197.862 Å	497.00 ± 99.50	497.00	1.00
Mg VII 280.737 Å	137.00 ± 27.30	137.00	1.00
Si VII 275.368 Å	441.00 ± 88.20	442.00	1.00
Fe X 184.536 Å	1720.00 ± 344.00	1720.00	1.00
Fe XI 188.216 Å	1580.00 ± 316.00	1580.00	1.00
Fe XII 192.394 Å	402.00 ± 181.00	404.00	1.00
Fe XI 180.401 Å	3100.00 ± 620.00	3100.00	1.00
S X 264.233 Å	82.80 ± 28.70	82.90	1.00
Si X 258.375 Å	685.00 ± 137.00	685.00	1.00
Fe XII 195.119 Å	1260.00 ± 675.00	1260.00	1.00
Fe XIII 202.044 Å	143.00 ± 810.00	143.00	1.00
Fe XIII 203.826 Å	367.00 ± 234.00	368.00	1.00
Fe XV 284.160 Å	94.80 ± 654.00	91.30	1.04
Fe XIV 270.519 Å	32.70 ± 66.40	32.40	1.01
Fe XIV 264.787 Å	69.90 ± 103.00	69.40	1.01
Fe XVI 262.984 Å	0.66 ± 24.00	0.59	1.11
S XIII 256.686 Å	1.59 ± 33.00	1.49	1.07
Ca XIV 193.874 Å	1.49e-02 ± 0.36	1.33e-02	1.12
Ca XV 200.972 Å	4.88e-04 ± 0.30	3.94e-04	1.24
Ca XVI 208.604 Å	2.06e-05 ± 0.30	4.60e-04	0.04
Ca XVII 192.858 Å	2.32e-06 ± 1.65	1.10e-02	0.00
Ti-poly	17.50 ± 19.50	17.10	1.02
Al-thick	1.48e-03 ± 0.30	8.31e-03	0.18

3. DISCUSSION

In the analysis section of this Letter, we have illustrated that the combined *Hinode* XRT and EIS data set has a blind spot in temperature–EM space and that the dimensions of the blind spot depend heavily on the temperature of the plasma along the line of sight. Here, we explain the origin of this blind spot. The emissivity functions of key EIS spectral lines are shown in the upper panel of Figure 3. The EIS instrument is able to detect plasma with temperatures up to 4 MK very well. At higher temperatures, EIS can observe the Ca XVII and many Fe XVII lines, but these lines are weak and blended with other transitions (Del Zanna et al. 2011; Del Zanna & Ishikawa 2009). During solar flares, EIS can also measure Fe XXIII and Fe XXIV lines (formed at temperatures $\gtrsim$ 10 MK), but in non-flaring active regions, these lines are normally blended with many other transitions (Del Zanna 2008; Del Zanna et al. 2011). The response curves of a few of the broadband XRT filters are shown in the middle panel of Figure 3. These filters are sensitive to a wide range of temperatures; ratios between the filters are used as a proxy for the temperature. The thickest filters are required to obtain knowledge of high-temperature plasma. Their efficiencies, however, are ~3 orders of magnitude lower than those of the thin filters, limiting the ability of these filter images to detect low EM plasma.

In an active region core, we determined that *Hinode* EIS and XRT cannot detect plasma with EMs less than 10^{27} cm^{-5} and $T \geqslant 6$ MK. Winebarger et al. (2011) determined that high-frequency heating could support temperatures up to 6 MK, while low-frequency heating would produce higher temperature plasma. This analysis suggests that *Hinode* EIS and XRT cannot be used to confirm the existence of high-temperature, low EM plasma, and hence cannot easily discriminate between low- and high-frequency heating in active region cores. If only cool emission is along the line of sight, the blind spot is the generally at lower EMs and temperatures, i.e., it is easier to detect high-temperature plasma if only cool plasma is along the line of sight. It is interesting to note that the previous analyses found evidence

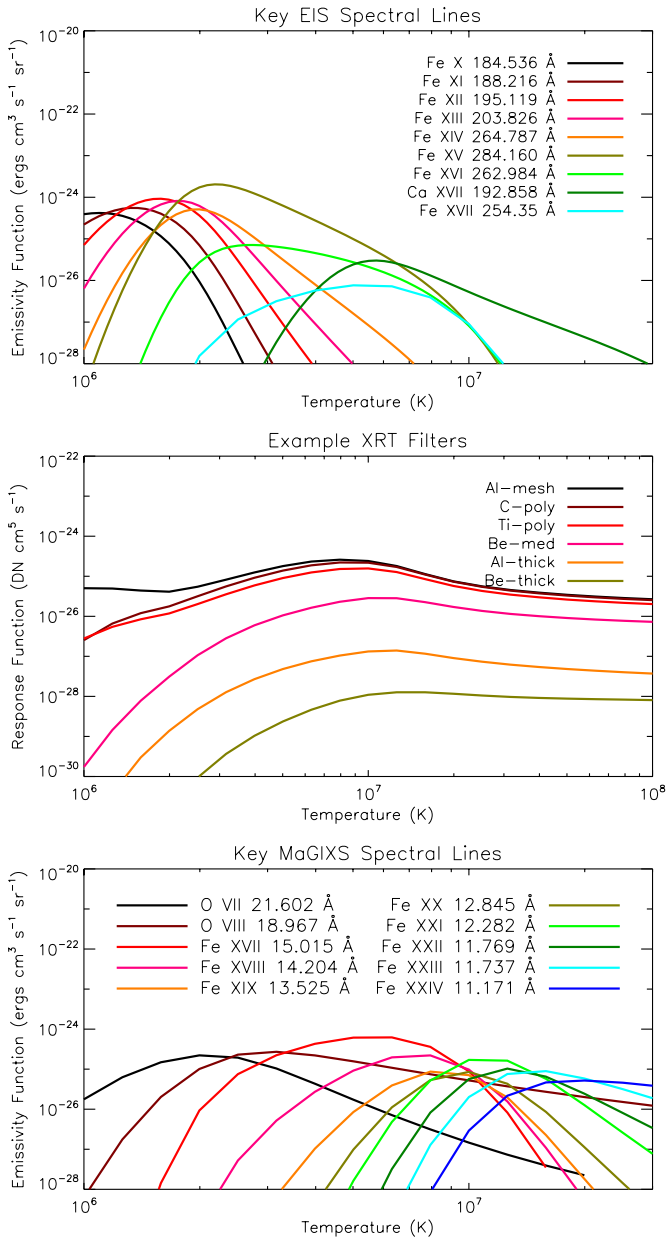

Figure 3. Top panel: the emissivity functions for key EIS spectral lines. Middle panel: the response functions for example XRT filters. Bottom panel: the emissivity functions of spectral lines in the 6–24 Å wavelength range to be observed by MaGIXS.

of high-temperature plasma in active regions, but away from the active region core (Schmelz et al. 2009a, 2009b; Reale et al. 2009). Those data sets included only X-ray observations.

To detect high-temperature, low EM plasma, we must observe a spatially and spectrally resolved solar spectrum that contains strong, high-temperature emission lines. The proposed MaGIXS (Kobayashi et al. 2010) will observe the solar spectrum at 6–24 Å. This wavelength range has a wide variety of strong spectral lines formed over a large temperature range ($6.2 < \log T < 7.2$). The emissivity functions of a few spectral lines to be observed by MaGIXS are shown in the lower panel of Figure 3. These spectral lines are stronger, have better high-temperature coverage, and provide better temperature discrimination than is currently available in EUV spectrometers or X-ray broadband filter imagers at high temperatures.

Hinode is a Japanese mission developed and launched by ISAS/JAXA, with NAOJ as domestic partner and NASA and STFC (UK) as international partners. It is operated by these agencies in cooperation with ESA and the NSC (Norway).

REFERENCES

Bradshaw, S. J., & Klimchuk, J. A. 2011, ApJS, 194, 26
Del Zanna, G. 2008, A&A, 481, L69
Del Zanna, G., & Ishikawa, Y. 2009, A&A, 508, 1517
Del Zanna, G., Mitra-Kraev, U., Bradshaw, S. J., Mason, H. E., & Asai, A. 2011, A&A, 526, A1
Dere, K. P., Landi, E., Young, P. R., et al. 2009, A&A, 498, 915
Feldman, U., Mandelbaum, P., Seely, J. F., Doschek, G. A., & Gursky, H. 1992, ApJS, 81, 387
Golub, L., Deluca, E. E., Sette, A., & Weber, M. 2004, in ASP Conf. Ser. 325, The Solar-B Mission and the Forefront of Solar Physics, ed. T. Sakurai & T. Sekii (San Francisco, CA: ASP), 217
Klimchuk, J. A. 2006, Sol. Phys., 234, 41
Klimchuk, J. A. 2009, in ASP Conf. Ser. 415, The Second Hinode Science Meeting: Beyond Discovery-Toward Understanding, ed. B. Lites, M. Cheung, T. Magara, J. Mariska, & K. Reeves (San Francisco, CA: ASP), 221
Klimchuk, J. A., Patsourakos, S., & Cargill, P. J. 2008, ApJ, 682, 1351
Kobayashi, K., Cirtain, J., Golub, L., et al. 2010, Proc. SPIE, 7732, 773233
Lang, J., Kent, B. J., Paustian, W., et al. 2006, Appl. Opt., 45, 8689
Martens, P. C. H., van den Oord, G. H. J., & Hoyng, P. 1985, Sol. Phys., 96, 253
Mulu-Moore, F. M., Winebarger, A. R., & Warren, H. P. 2011, ApJ, 742, L6
Narukage, N., Sakao, T., Kano, R., et al. 2011, Sol. Phys., 269, 169
Parker, E. N. 1972, ApJ, 174, 499
Reale, F., Testa, P., Klimchuk, J. A., & Parenti, S. 2009, ApJ, 698, 756
Schmelz, J. T., Kashyap, V. L., Saar, S. H., et al. 2009a, ApJ, 704, 863
Schmelz, J. T., Saar, S. H., DeLuca, E. E., et al. 2009b, ApJ, 693, L131
Shestov, S. V., Kuzin, S. V., Urnov, A. M., Ul'Yanov, A. S., & Bogachev, S. A. 2010, Astron. Lett., 36, 44
Warren, H. P., Brooks, D., & Winebarger, A. R. 2011, ApJ, 734, 90
Weber, M. A., Deluca, E. E., Golub, L., & Sette, A. L. 2004, in IAU Symp. 223, Multi-Wavelength Investigations of Solar Activity, ed. A. V. Stepanov, E. E. Benevolenskaya, & A. G. Kosovichev (Cambridge: Cambridge Univ. Press), 321
Winebarger, A. R., Schmelz, J. T., Warren, H. P., Saar, S. H., & Kashyap, V. L. 2011, ApJ, 740, 2